Semiclassical calculations for the ^{156}Gd (p,d) reaction

Hafez A. Radi,[1,2,*] John O. Rasmussen,[2,†] and Raul J. Donangelo[3,‡]

[1]*October University for Modern Sciences and Arts (MSA), Faculty of Engineering, Giza, Egypt*

[2]*University of California at Berkeley, Lawrence Berkeley National Lab, Nuclear Science Division, California 94720, USA*

[3]*Instituto de Fısica, Facultad de Ingenieria, C.C. 30, C.P. 11000, Montevideo, Uruguay*

(Received 16 May 2017; revised manuscript received 27 June 2017; published 1 September 2017)

Numerical semiclassical calculations are carried out to study the angular distribution of deuterons from the p,d pickup reaction of 25 MeV protons incident on the nucleus ^{156}Gd and also its proton elastic scattering. It is found that, due to the rapid fall of the real optical potential in the vicinity of the target nucleus, the classical trajectories are very sensitive to the proton impact parameters. A selection of 276,983 trajectories is used for protons with impact parameters b_p satisfying 7.23018 fm $\leqslant b_p \leqslant$ 10 fm with steps of 10^{-5} fm. Using the imaginary part of the optical potential for protons, a simple quantum approach is constructed to evaluate the probability of a surviving proton throughout its path. In addition, a simple three-body quantum approach is developed to calculate the probability of a neutron transfer by a surviving proton at closest approach. The formed deuteron is then allowed to start its trajectory while keeping its identity until detected. Throughout this journey, the deuteron trajectory is under the influence of its Coulomb and real optical potential, while its absorption is determined by the imaginary optical potential component. Within estimated uncertainties, the resulting theoretical angular distribution achieves a comparable fit with experimental results for the angular momentum transfer L = 0 compared to other theoretical models, and concludes that the strong p,d cross sections are due to the dominant $s_{1/2}$ component of the Nilsson $\frac{1}{2}^+$[400] level in ^{155}Gd.

DOI: 10.1103/PhysRevC.96.034602

I. INTRODUCTION

Serious efforts have been made in recent years for the measurement of nuclear-reactions involving deformed nuclei. Still, a large amount of information and theoretical questions remain.

Inspired by the doctoral thesis of Tim Ross [1] under the guidance of Prof. Con Beausang, and the data in their three publications with colleagues [2–4], we have undertaken to develop a semiclassical theoretical model to both the ^{156}Gd (p,p) and ^{156}Gd (p,d) reactions. The experimental data mostly come from collaboration at cyclotrons at Lawrence Berkeley National Lab and at Texas A & M cyclotron in College Station, TX. Unlike Ref. [5], where a neutron is considered to form a compound nucleus, we avoided considering cases when protons with small impact parameters interact with the rotational Gd nucleus to form a compound nucleus.

Also, in this study we treated semiclassical calculations for both neutron-pickup and elastic scattering for 25 MeV protons incident on ^{156}Gd nuclei. With this model, we did not attempt to calculate a two-neutron pick-up and compare it with other work [6–8].

It is rare to consider semi-classical calculations as a solution to the problem at hand. However, considerable theoretical classical-trajectory calculations have produced reliable results in many studies such as Radi *et al.* [9].

Here we make comparison with DWBA angular distribution results in earlier publications [4,10].

Experimental p,d relative cross sections for Gd targets, labeled by the mass number of the final nucleus, are shown in Fig. 1 (see Fig. 63 of Ref. [1]). This figure shows that the $\frac{1}{2}^+$[400] band is the most highly populated in ^{155,157}Gd via the (p,d) reaction.

We attempt to rationalize some of the patterns of Fig. 2 [4,10], but without invoking the double-BCS model of Chu *et al.* [6], in which the BCS equations are applied separately to the upgoing and downgoing Nilsson levels as quadrupole deformation increases. We note the dominance of orbitals $\frac{1}{2}^+$[400] and $\frac{3}{2}^+$[402] from below the 82-shell gap. They both have substantial wave functions at the north and south poles of the target nucleus.

The p,d reaction states $\frac{1}{2}^+$[400] in ^{155,157}Gd and their relative intensities of Refs. [4,10], are shown in Table I.

Motivated by these results and the fact that the wavelength of the incoming proton is considerably smaller than the nuclear size, we can simplify the theoretical treatment of L = 0 for the ^{156}Gd target by considering a semiclassical approach as denoted previously. Also, the code developed by this treatment is simpler than earlier computer program codes: such as the DWUCK [11], CHUCK [12], PTOLEMY [13], and FRESCO [14] codes.

II. NUCLEAR DEFORMATION AND POTENTIAL

The p,d reaction of a 25 MeV proton with ^{156}Gd is mainly a peripheral one. This will be evident from this study. We consider quadrupole and hexadecapole deformations of a prolate spheroidal Gd nucleus. When an angle χ is measured from the nuclear major axis, the radius of the nucleus at any angle $0 \leqslant \chi \leqslant \pi$ is given by

$$R_T(\chi) = R_{To}[1 + \beta_2 Y_{20}(\chi) + \beta_4 Y_{40}(\chi)], \qquad (1)$$

*hradi@msa.eun.eg

†oxras@berkeley.edu

‡donangel@fing.edu.uy

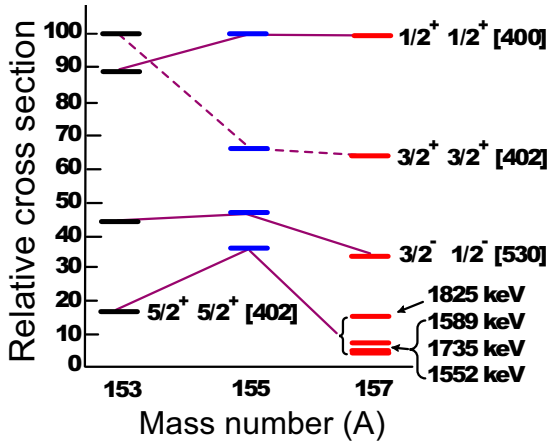

FIG. 1. Relative cross sections for p,d reactions on three even-even Gd targets (from Ross *et al.* [2]). The excitation energy of the Nilsson band-head energies for ^{155}Gd are also taken from data in Allmond *et al.* [10] work.

where we used the monopole radius $R_{To} = r_o A_T^{1/3}$ (with $r_o \simeq 1.2$ fm [15,16]), $\beta_2 = 0.271$, and $\beta_4 = 0.088$ [17]. In addition, we assume that transfer occurs at the point of closest approach (CA), which is indicated by a distance r_{CA} from the center of the target nucleus (see Fig. 3). In the lab, we consider a stationary ^{156}Gd target nucleus and a proton coming from infinity at $t = 0$ with a speed v_p and impact parameter b_p (see Fig. 3).

The simplest spherical liquid-drop density model is given by a constant nucleon density ρ_o out to a radius R_T. For a nucleus of any mass number A_T, this density has nearly the value $\rho_o = 0.138$ nucleon/fm^3 [18–20]. The sharp-surface model can be improved if we allow the surface to be diffuse. This can be done by considering the following well-known, two-parameter Wood-Saxon distribution [21]:

$$\rho_T(r) = \frac{\rho_o}{1 + e^{(r-R_T)/a}} [a = \text{nuclear diffuseness}]. \quad (2)$$

The value of a determines the nuclear-skin thickness $t = 4a \ln 3$, at which $\rho_T(r)$ decreases from $0.9\rho_o$ to $0.1\rho_o$. From Atomic Data and Nuclear Data Tables, we take the value $a = 0.576$ fm [21–25], which gives $t = 2.53$ fm. For a deformed ^{156}Gd with $R_{To} = r_o A_T^{1/3} = 6.46$ fm, Eq. (1) gives a major axis (north pole) with value $(R_T)_{max} = 8.045$fm and a minor axis (equator) with value $(R_T)_{min} = 6.088$fm. Figure 4 shows the variation of nuclear density along the major axis (a) and minor axis (b).

TABLE I. Experimental results from TABLE III of Ref. [10] and Table VII of Ref. [4]. The relative yields for levels directly populated by the ^{156}Gd(p,d)^{155}Gd and ^{158}Gd(p,d)^{157}Gd reactions are indicated. Yields (I_{rel}) are shown relative to the state with the highest cross section, the $\frac{1}{2}^+$[400]. Relative yields are measured between 33° and 55° with respect to the beam axis.

Nucleus	E^*(keV)	I_{rel}	J^π	$\Omega^\pi[Nn_z\Lambda]$
^{155}Gd	367.66 (27)	100(16)	$\frac{1}{2}^+$	$\frac{1}{2}^+$[400]
^{157}Gd	682.90 (4)	100(4)	$\frac{1}{2}^+$	$\frac{1}{2}^+$[400]

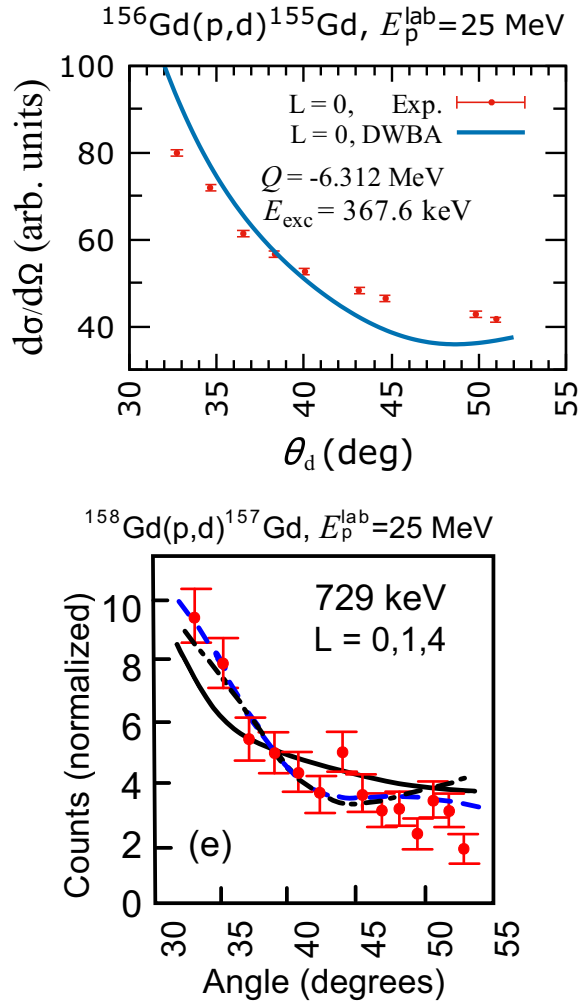

FIG. 2. (Top) The experimental angular momentum transfer L = 0 data of Allmond *et al.* [10] and L = 0 DWBA [11] angular distributions for the direct population of the 367 keV, $\frac{1}{2}^+$[400]. (Bottom) The experimental data of the level 729 keV are the colored dots with error bars and are taken from Fig. 7(e) of Ross *et al.* [4]. The graph shows the DWBA angular distributions fit which is best characterized by L = 0,1,4. The three different L values are: solid black for L = 0; colored line running through the highest point for L = 1, and a dot-dash black line for L = 4.

For a general treatment of the problem, we consider the reaction T(p,o)R, where T is the ^{156}Gd target nucleus (mass m_T), p is the incoming proton (mass m_p), o is the outgoing particle (mass m_o), and R is the residual nucleus (mass m_R). The center of mass (c.m.) of the system has a constant velocity $v_{pT}^{c.m.} = (m_p v_p)/m_{tot}$, where m_{tot} is the total mass of the system. The initial lab kinetic energy of the proton is $K_p^{lab} (= E_p^{lab}) = \frac{1}{2} m_p v_p^2$. Therefore, the initial kinetic energy of the system in the center of mass frame is

$$K_{pT}^{c.m.} = \tfrac{1}{2} m_{tot} \left(v_{pT}^{c.m.}\right)^2. \quad (3)$$

The initial relative kinetic energy is the difference between the two energies and will be the energy available for the

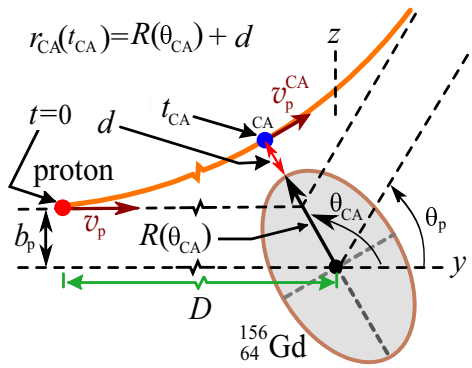

FIG. 3. Schematic diagram for the scattering trajectory of a proton on a deformed Gd nucleus (exaggerated scale).

collision of the proton with the target nucleus. Thus,

$$E_{\rm pT}^{\rm c.m} = \tfrac{1}{2}\mu_{\rm pT}\, v_{\rm p}^2, \tag{4}$$

where $\mu_{\rm pT} = m_{\rm p} m_{\rm T}/(m_{\rm p}+m_{\rm T})$ is the reduced mass of the proton (p) colliding with the target nucleus (T).

For (p,p) and (p,d) reactions, conservation of energy of the system for the incoming (in) and outgoing (out) channels leads to

$$E_{\rm pT}^{\rm c.m.} = \tfrac{1}{2}\mu_{\rm pT}\, v_{\rm p}^2 = \begin{cases} \tfrac{1}{2}\mu_{\rm pT}\, v^2 + U_{\rm pT}\big(r, E_{\rm p}^{\rm lab}\big), & \text{[in \& out]} \\ \tfrac{1}{2}\mu_{\rm oR}\, v^2 + U_{\rm oR}\big(r, E_{\rm o}^{\rm lab}\big), & \text{[out]} \end{cases}, \tag{5}$$

where v is the speed at any distance r from the center of the nucleus ($r_{\rm CA} \leqslant r \leqslant \infty$) for the proton or the outgoing particle. For classical trajectories, the terms $U_{\rm pT}$ and $U_{\rm oR}$ are the total Coulomb plus only the ***real*** part of the optical potentials

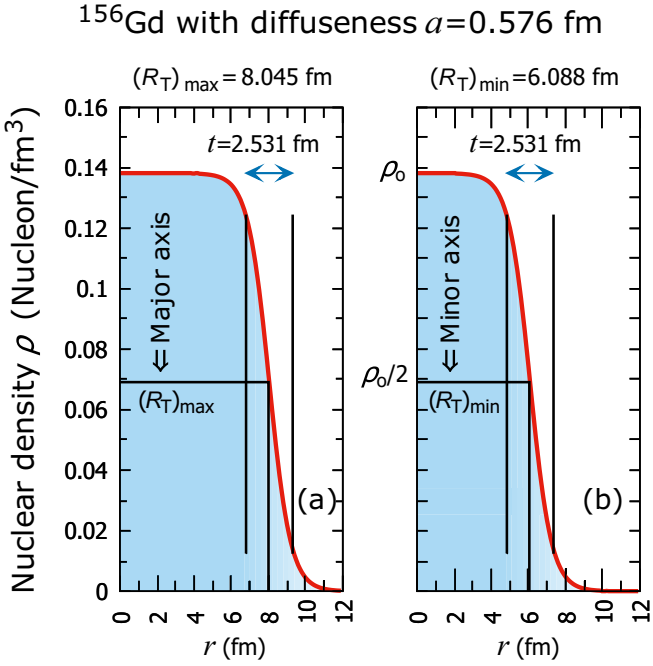

FIG. 4. (a) Variation of the nuclear density of a ^{156}Gd nucleus along the major axis and (b) along the minor axis.

for the proton-target interacting system and outgoing-residual interacting system, respectively.

Based on the C. Perey and F. Perey [26] compilation, this potential depends on the energy of the interacting particle and the constituents of the nucleus. The total potential can be written as a sum of a Coulomb-potential term plus a complex optical-potential term. For the proton interaction, we have

$$U_{\rm pT}\big(r, E_{\rm p}^{\rm lab}\big) = V_{\rm pT}^{\rm C}(r) + V_{\rm pT}^{\rm Opt}\big(r, E_{\rm p}^{\rm lab}\big) + i\, W_{\rm pT}^{\rm Opt}\big(r, E_{\rm p}^{\rm lab}\big). \tag{6}$$

For a proton interacting with a nucleus of atomic number $Z_{\rm T}$ and mass number $A_{\rm T}$, a uniform spherical charge distribution is considered [26] for the Coulomb term by taking the nuclear radius to be $R_{\rm p}^{\rm C} = r_{\rm p}^{\rm C} A_{\rm T}^{1/3}$, with $r_{\rm p}^{\rm C} = 1.25$ fm. Thus,

$$V_{\rm pT}^{\rm C}(r) = \begin{cases} \dfrac{1}{4\pi\epsilon_{\rm o}} \dfrac{Z_{\rm p} Z_{\rm T} e^2}{r} & \big(r \geqslant R_{\rm p}^{\rm C}\big) \\ \dfrac{1}{4\pi\epsilon_{\rm o}} \dfrac{Z_{\rm p} Z_{\rm T} e^2}{2R_{\rm p}^{\rm C}} \left(3 - \dfrac{r^2}{\big(R_{\rm p}^{\rm C}\big)^2}\right) & \big(r \leqslant R_{\rm p}^{\rm C}\big) \end{cases}. \tag{7}$$

Here we accept the nondependence of the quadrupole and hexadecapole contributions to the Coulomb interaction.

The real part of the optical potential contains a spin-independent central potential (indicated by the superscript "ce") plus a spin-orbit potential (indicated by the superscript "so"). Based on Ref [26], the real and imaginary parts of the optical potential can be written as

$$V_{\rm pT}^{\rm Opt}\big(r, E_{\rm p}^{\rm lab}\big) = -V_{\rm pT}^{\rm ce}\big(E_{\rm p}^{\rm lab}\big) f\big(x_{\rm pT}^{\rm ce}\big) - \tfrac{2}{r\, a_{\rm p}^{\rm so}} V_{\rm p}^{\rm so} e^{x_{\rm pT}^{\rm so}} f^2\big(x_{\rm pT}^{\rm so}\big), \tag{8}$$

$$W_{\rm pT}^{\rm Opt}\big(r, E_{\rm p}^{\rm lab}\big) = -W_{\rm p} f\big(x_{\rm pT}^{\rm W}\big) - 4 W_{\rm pT}^{D}\, e^{x_{\rm pT}^{\rm D}} f^2\big(x_{\rm pT}^{\rm D}\big), \tag{9}$$

$$\text{where} \quad \left.\begin{aligned} f\big(x_{\rm pT}^{\rm n}\big) &= 1/\big[1 + e^{x_{\rm pT}^{\rm n}}\big], \\ x_{\rm pT}^{\rm n} &= \big(r - r_{\rm p}^{\rm n}\, A_{\rm T}^{1/3}\big)/a_{\rm pT}^{\rm n} \end{aligned}\right\} (\rm n = ce,\ so,\ W,\ D). \tag{10}$$

In case of an outgoing particle o (deuteron, tritium, etc.) interacting with a residual nucleus R, a similar relation to Eqs. (6)–(10) holds, except the subscript pT is replaced by the subscript oR. Thus,

$$U_{\rm oR}\big(r, E_{\rm o}^{\rm lab}\big) = V_{\rm oR}^{\rm C}(r) + V_{\rm oR}^{\rm Opt}\big(r, E_{\rm o}^{\rm lab}\big) + i\, W_{\rm oR}^{\rm Opt}\big(r, E_{\rm o}^{\rm lab}\big). \tag{11}$$

Table II [26] lists the parameters of the proton's optical potential for the real part and imaginary part, Eq. (6). Table III [26,27] lists the parameters used in the optical potential when the outgoing particle is a deuteron (d) interacting with a residual nucleus ${}^{A_R}_{Z_R}{\rm R}_{N_R}$, Eq. (11). In the deuteron case, the parameters that have no values are indicated by the symbol ∅. We used the monopole radius $R_{\rm Ro} = r_{\rm o} A_{\rm R}^{1/3}$ with Refs. [15,16]. For displaying the residual nucleus shape, ^{155}Gd, we will use $\beta_2 = 0.252$, and $\beta_4 = 0.083$ [17].

Figure 5 shows the results of using the real parameters of Tables II and III in calculating the real optical potential for ^{156}Gd(p,p)^{156}Gd, Eq. (6), and ^{156}Gd(p,d)^{155}Gd, Eq. (11), when $E_{\rm p}^{\rm lab} = 25$ MeV.

Figure 5 indicates that the attractive real optical potential is of the order of −5MeV when the proton touches the nuclear

TABLE II. Optical potential parameters used when a proton interacts with a target nucleus ${}^{A_T}_{Z_T}\mathrm{T}_{N_T}$ [26].

$V_{\mathrm{pT}}^{\mathrm{ce}}$	$[54-0.32\,E_{\mathrm{p}}^{\mathrm{lab}}+24(N_{\mathrm{T}}-Z_{\mathrm{T}})/A_{\mathrm{T}}+0.4(Z_{\mathrm{T}}/A_{\mathrm{T}}^{1/3})]$ MeV	$r_{\mathrm{p}}^{\mathrm{ce}}$	1.17 fm	$a_{\mathrm{p}}^{\mathrm{ce}}$	0.75 fm
$V_{\mathrm{p}}^{\mathrm{so}}$	6.2 MeV	$r_{\mathrm{p}}^{\mathrm{so}}$	1.01 fm	$a_{\mathrm{p}}^{\mathrm{so}}$	0.75 fm
W_{p}	$[0.22\,E_{\mathrm{p}}^{\mathrm{lab}}-2.7]$ MeV	$r_{\mathrm{p}}^{\mathrm{W}}$	1.32 fm	$a_{\mathrm{pT}}^{\mathrm{W}}$	$[0.51+0.7\,(\mathrm{N_T}-Z_{\mathrm{T}})/A_{\mathrm{T}}]$ fm
$W_{\mathrm{pT}}^{\mathrm{D}}$	$[11.8-0.25\,E_{\mathrm{p}}^{\mathrm{lab}}+12(\mathrm{N_T}-Z_{\mathrm{T}})/A_{\mathrm{T}}]$ MeV	$r_{\mathrm{p}}^{\mathrm{D}}$	1.32 fm	$a_{\mathrm{pT}}^{\mathrm{D}}$	$[0.51+0.7(\mathrm{N_T}-Z_{\mathrm{T}})/A_{\mathrm{T}}]$ fm
		$r_{\mathrm{p}}^{\mathrm{C}}$	1.25 fm		

surface at the north pole and we assume a sharp-nuclear-surface of the target. If the proton touches the equator, the optical potential goes to a much greater negative value of about −33 MeV. Therefore, a peripheral reaction near the equator is much less probable due to the strength of the nuclear attraction. When we study proton trajectories with different impact parameters, we will find that a peripheral reaction is more probable near the north and south poles of the prolate nucleus.

For deuterons, Fig. 5 shows that the attractive real optical potential is of the order of −10 MeV when the deuteron is formed at the north pole of the nuclear surface. If the deuteron is formed near the equator, where the real optical potential is about −52 MeV, then one should expect that the deuteron will be attracted to the residual nucleus.

III. PROTON AND DEUTERON TRAJECTORIES

In addition to energy conservation given by Eq. (5), the angular momentum of the proton with respect to the c.m. is also considered to be conserved. This approximation is accepted for grazing trajectories since the nuclear potential has a small effect on the conservation of angular momentum. We use the relation between the magnitude of the proton's angular momentum at the initial point $(r_{\mathrm{i}},\theta_{\mathrm{i}})$ and at any point (r,θ) (see Fig. 3) and applying the real upper part of Eq. (5), to find the following:

$$\frac{dr}{dt}=\pm\frac{v_{\mathrm{p}}\,b_{\mathrm{p}}}{r^2}F_{\mathrm{pT}}\left(r,b_{\mathrm{p}},E_{\mathrm{p}}^{\mathrm{lab}}\right),\quad\text{and}\tag{12}$$

$$\frac{dr}{d\theta}=\pm\,F_{\mathrm{pT}}\left(r,b_{\mathrm{p}},E_{\mathrm{p}}^{\mathrm{lab}}\right),\tag{13}$$

where the function F_{pT} depends on the proton's position, impact parameter, lab energy, the kind of target nucleus under consideration, and can be written as

$$F_{\mathrm{pT}}\left(r,b_{\mathrm{p}},E_{\mathrm{p}}^{\mathrm{lab}}\right)=\frac{r^2}{b_{\mathrm{p}}}\sqrt{\left[1-\left(\frac{b_{\mathrm{p}}}{r}\right)^2\right]-\frac{\mathrm{Re}\left[U_{\mathrm{pT}}\left(r,E_{\mathrm{p}}^{\mathrm{lab}}\right)\right]}{E_{\mathrm{pT}}^{\mathrm{c.m.}}}}.\tag{14}$$

Equation (13) is an ordinary first-order differential equation that cannot be solved analytically due to the existence of a complicated potential in the square root of the right-hand side of Eq. (14). On the other hand, Eq. (13) can be solved numerically for the incoming-proton channel and/or the outgoing-proton or -deuteron channels.

For the incoming channel with an impact parameter b_{p}, we start from an initial large angle $\theta_{\mathrm{i}}=179.96^{\circ}$ and calculate the initial values (see Fig. 3):

$$\begin{aligned}r_{\mathrm{i}}&=b_{\mathrm{p}}/\sin(\pi-\theta_{\mathrm{i}})>10{,}000\text{ fm},\\ D&=b_{\mathrm{p}}/\tan(\pi-\theta_{\mathrm{i}})>10{,}000\text{ fm}.\end{aligned}\tag{15}$$

Then we integrate Eq. (13) until we reach the point of closest approach $(r_{\mathrm{CA}},\theta_{\mathrm{CA}})$, i.e., $(\theta_{\mathrm{i}}\leqslant\theta\leqslant\theta_{\mathrm{CA}})$. Since both r and θ decrease in the incoming channel, the positive sign of Eq. (13) is selected. Thus,

$$\frac{dr}{d\theta}=+F_{\mathrm{pT}}\left(r,b_{\mathrm{p}},E_{\mathrm{p}}^{\mathrm{lab}}\right)\text{ (incoming proton)}.\tag{16}$$

When the proton reaches the point of CA, its velocity will be tangent to its trajectory and the condition $dr/d\theta|_{\mathrm{CA}}=0$ must be fulfilled. This will lead to the following relation:

$$b_{\mathrm{p}}=r_{\mathrm{CA}}\sqrt{1-\frac{\mathrm{Re}\left[U_{\mathrm{pT}}\left(r_{\mathrm{CA}},E_{\mathrm{p}}^{\mathrm{lab}}\right)\right]}{E_{\mathrm{pT}}^{\mathrm{c.m.}}}}.\tag{17}$$

For the outgoing-proton channel, we start from the point of closest approach $(r_{\mathrm{CA}},\theta_{\mathrm{CA}})$ and integrate Eq. (13) to the final values $(r_{\mathrm{f}},\theta_{\mathrm{f}})$, where $r_{\mathrm{f}}\approx 2\times10^6$ fm and $\theta_{\mathrm{CA}}\leqslant\theta\leqslant\theta_{\mathrm{f}}$. Since r increases while θ decreases, the negative sign of Eq. (13) must be selected. Thus,

$$\frac{dr}{d\theta}=-F_{\mathrm{pT}}\left(r,b_{\mathrm{p}},E_{\mathrm{p}}^{\mathrm{lab}}\right)\text{ (outgoing proton)}.\tag{18}$$

We consider cases for a particular range of b_{p} that produces CA points that lie within the short-range-tails of the nuclear matter. When a proton (p) reaches the point of CA at a distance r_{CA}, there is a chance that this proton can pick up a neutron. Then, the c.m. energy of the formed deuteron (d) in

TABLE III. The optical-model parameters used when a deuteron interacts with a residual nucleus ${}^{A_R}_{Z_R}\mathrm{R}_{N_R}$ [26,27].

$V_{\mathrm{dR}}^{\mathrm{ce}}$	$[81-0.22\,E_{\mathrm{d}}^{\mathrm{lab}}+2(Z_{\mathrm{R}}/A_{\mathrm{R}}^{1/3})]$ MeV	$r_{\mathrm{d}}^{\mathrm{ce}}$	1.15 fm	$a_{\mathrm{d}}^{\mathrm{ce}}$	0.81 fm
$V_{\mathrm{d}}^{\mathrm{so}}$	Ø	$r_{\mathrm{d}}^{(\mathrm{so})}$	Ø	$a_{\mathrm{d}}^{\mathrm{so}}$	Ø
$W_{\mathrm{d}}^{\mathrm{D}}$	$[14.4-0.24\,E_{\mathrm{d}}^{\mathrm{lab}}]$ MeV	$r_{\mathrm{d}}^{\mathrm{D}}$	1.34 fm	$a_{\mathrm{d}}^{\mathrm{D}}$	0.68 fm
		$r_{\mathrm{d}}^{\mathrm{C}}$	1.15 fm		

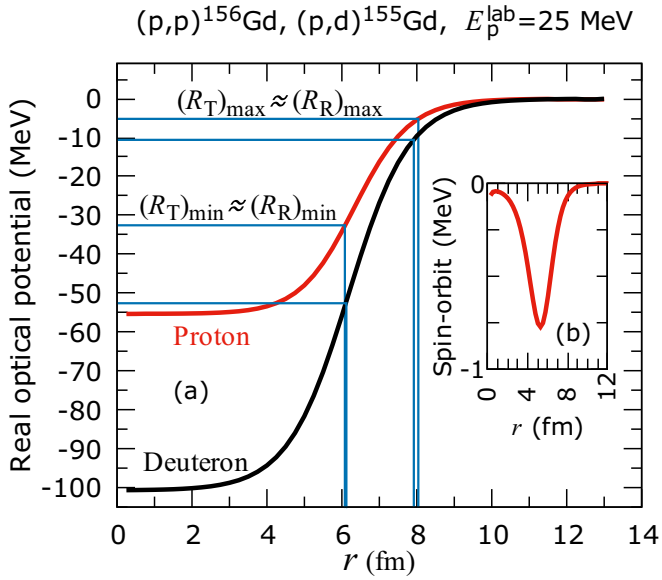

FIG. 5. (a) Values of the real optical potential (central + spin-orbit) for protons (red) and deuterons (black) [26]. The assumed sharp maximum and minimum radii of the target and residual nuclei and their corresponding potential values are displayed. (b) The small contribution of the spin-orbit term to the total real optical potential for protons is displayed in a smaller window.

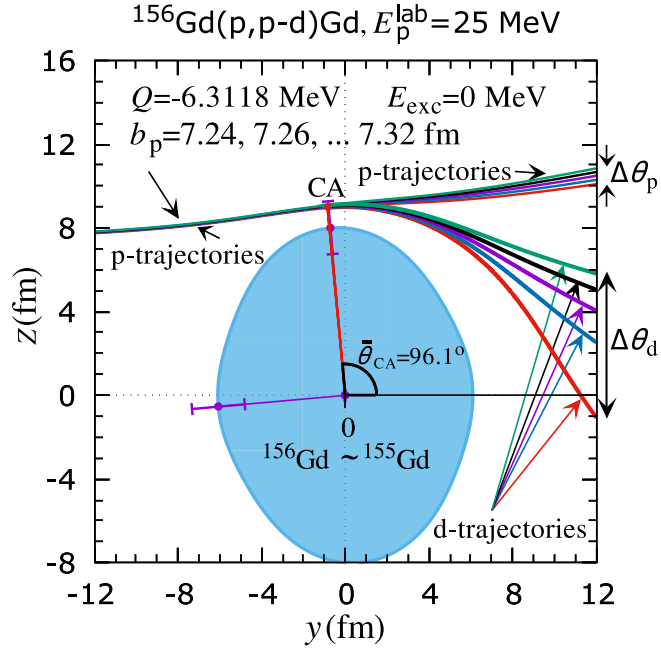

FIG. 6. The figure shows five incoming proton trajectories with a difference of 0.02 fm between each value of b_p. After the CA, the outgoing proton trajectories acquire a small range of deflection $\Delta\theta_p$. If the proton picks up a neutron at CA, the range of deuteron deflection $\Delta\theta_d$ is much bigger than $\Delta\theta_p$ due to the greater attraction of the nuclear potential at the CA.

the outgoing channel will be

$$E_{dR}^{c.m.} = E_{pT}^{c.m.} + Q - E_{exc}, \tag{19}$$

where Q is the Q-value of the T(p,d)R reaction and E_{exc} is the excitation energy of the residual nucleus R. This c.m. energy $E_{dR}^{c.m.}$ must correspond to a deuteron coming from infinity with a speed v_d, impact parameter b_d, and lab energy E_d^{lab} given by

$$E_d^{lab} = (m_d + m_R)\left(E_{pT}^{c.m.} + Q - E_{exc}\right)/m_R. \tag{20}$$

Thus, in the deuteron-outgoing channel, we start from the CA of the deuteron and solve the differential equation:

$$\frac{dr}{d\theta} = -F_{dR}\left(r, b_d, E_d^{lab}\right) \text{(outgoing deuteron)}, \tag{21}$$

where the function F_{dR} depends on the position, energy, the calculated impact parameter of the deuteron (as well as the constituents of the residual nucleus R), and is given by:

$$F_{dR}\left(r, b_d, E_d^{lab}\right) = \frac{r^2}{b_d}\sqrt{\left[1 - \left(\frac{b_d}{r}\right)^2\right] - \frac{\mathrm{Re}\left[U_{dR}\left(r, E_d^{lab}\right)\right]}{E_{dR}^{c.m.}}}. \tag{22}$$

Additionally, we consider the deuteron's CA point to coincide with the proton's CA point, i.e., r_{CA} is common to both the proton and deuteron trajectories at a given impact parameter. At this point, the deuteron's velocity will be tangent to its trajectory and the condition $dr/d\theta|_{CA} = 0$ for the outgoing deuteron must be fulfilled. This will lead to the following relation for b_d:

$$b_d = r_{CA}\sqrt{1 - \frac{\mathrm{Re}\left[U_{dR}\left(r_{CA}, E_d^{lab}\right)\right]}{E_{dR}^{c.m.}}}. \tag{23}$$

The numerical solutions of Eq. (18) produce proton trajectories that penetrate the nuclear matter when the impact parameters satisfies $b_p \leqslant 6.911227$ fm. For the range $6.911228\,\text{fm} < b_p < 6.912695\,\text{fm}$, the proton's trajectories will not penetrate the nuclear matter, but produce the proton's final deflection that is less than $-90°$. Of course, these protons cannot be detected. For an impact satisfying $6.912695\,\text{fm} \leqslant b_p \leqslant 7.076\,\text{fm}$, we get deflections in the range $-90° \leqslant \theta_p \leqslant 0°$.

The restriction established for proton trajectories also applies to deuterons at the CA if $b_p < 7.229271$ fm. This results from satisfying the condition of choosing one common point for the proton's and deuteron's CA, as if forcing the deuteron to come from infinity and reach this particularly common value r_{CA}. From $b_p = 7.229271\,\text{fm}$ to the value $b_p < 7.230175\,\text{fm}$, the solution produces deuterons at CA but with final angles less than $\theta_d < -90°$. We get deuterons in the forward direction when the proton's impact satisfies $b_p \geqslant 7.23018$ fm. This allows us to conclude that the neutron pick-up process occurs mostly near the poles of the nucleus for this value of energy $E_p^{lab} = 25\,\text{MeV}$.

Figure 6 displays the proton's trajectories when only five selected impact parameters are chosen, $b_p = 7.24$, 7.26, 7.28, 7.30, and 7.32 fm. At the point of CA, we considered the possibility that the incoming proton trajectory might either continue as an outgoing proton trajectory, or result in an outgoing deuteron trajectory when the proton picks up a neutron. So, Fig. 6 displays both possibilities of existence. The range of the proton deflection angle $\Delta\theta_p$ is relatively small (from 9.45° to about 12.65°);while due to the relatively strong attractive optical potential, the range of the deuteron deflection

angle $\Delta\theta_d$ is relatively larger (from -58.5° to -12.45°). In the same figure we represent the point of the CA by a small red dot. At this point, and for the five selected impact parameters, the average Coulomb potential is about 10 MeV and the average real optical potential for the protons and deuterons are respectively about -1.5 MeV and -2.9 MeV. As expected, protons with big impact parameters, $b_p > 10$ fm, will suffer small deflections and their chance to pick-up a neutron from the Gd nucleus is extremely small. On the other hand, if the proton encountered the nucleus from the south pole, the angles of the outgoing protons will be *negative*, while the deuteron angles will be *positive*. In this work we consider only protons with impact parameters that lie in the yz plane and above the y axis. Rotating the y axis by 90 degrees produces trajectories that can be viewed experimentally in an xz plane.

At $\bar{\alpha} = \bar{\theta}_{CA} = 96.1^\circ$, if the proton deflects without picking up a neutron, the nucleus remains ^{156}Gd. However, if the proton picks up a neutron, the nucleus becomes ^{155}Gd. Since the size of ^{156}Gd is almost identical to ^{155}Gd, the nucleus drawn in Fig. 6 can be taken to represent either.

Table IV lists the values of the parameters used and quantities obtained to assemble Figure 6. For the elastic ^{156}Gd(p,p)^{156}Gd reaction, the common values used for the calculations are $E_p^{lab} = 25$ MeV and $E_{p\,Gd}^{c.m.} = 24.84$ MeV. In addition, for the ^{156}Gd(p,d)^{155}Gd reaction, the common values used for the calculations are $E_{d\,Gd}^{c.m.} = 18.529$ MeV and $E_d^{lab} = 18.768$ MeV. The last two values are based on Eqs. (19) and (20) after taking $Q = -6.312$ MeV.

We calculated 276,983 trajectories for protons with impact parameters satisfying $7.23018\,\text{fm} \leqslant b_p \leqslant 10\,\text{fm}$ with steps of 10^{-5}fm. This range of b_p is suitable for forming deuterons since r_{CA} values lie in the nuclear tail.

Figure 7(a) shows the variation of the proton's final deflection angle θ_p with respect to b_p. All deflection angles have positive values with a maximum of about 22.6° at about 8.5 fm.

Figure 7(b) shows the variations of the deuteron final deflection θ_d with b_p (assuming deuterons are produced in this range). For $7.235\,\text{fm} \leqslant b_p \leqslant 7.41\,\text{fm}$, the deuteron angles are negative and increase rapidly in the range $-89^\circ \leqslant \theta_d \leqslant 0^\circ$. After that region, θ_d reaches a maximum of about 26° at about 8.9 fm. Then, θ_d starts to decrease slightly with increasing b_p.

The attempts made in Fig. 7 should be supplemented with a quantum study (in the next sections) to calculate the probability of forming a deuteron at the CA, and also to consider the proton and deuteron absorption due to the imaginary part of the optical potential.

TABLE IV. Different values of b_p and their resulting final values as depicted in Fig. 6.

b_p (fm)	θ_p (deg)	b_d (fm)	θ_d (deg)	r_{CA}(fm)	α (deg)
7.24	10.32	7.024	−47.68	8.99	95.4
7.26	11.11	7.025	−29.59	9.03	95.8
7.28	11.82	7.027	−20.93	9.06	96.2
7.30	12.45	7.029	−15.20	9.09	96.5
7.32	13.11	7.033	−10.89	9.12	96.8

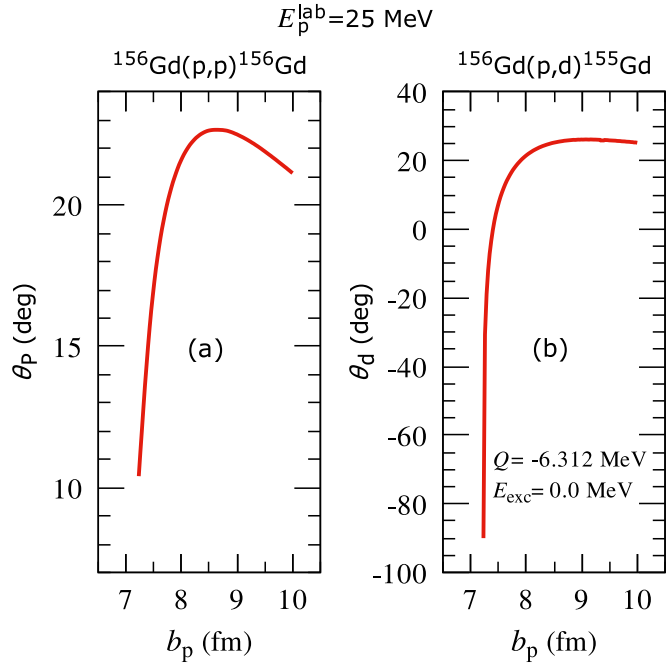

FIG. 7. Final deflection angles of 276,983 protons and deuterons with respect to the proton impact parameter.

IV. SPHERICAL SQUARE-WELL POTENTIAL APPROXIMATION

To introduce quantum-mechanical effects into this theoretical treatment, we employ a simple description for the neutron-tunneling process, avoiding complicated nuclear potentials as in Ref. [28], target deformations as in Ref. [15], and detailed analysis of neutron orbitals based on realistic Nilsson diagrams based on a rounded Wood-Saxon potential [29]. This is done by assuming a spherical square well for the neutron-nucleus potential of the heavy nucleus (referred to as 1) and neutron-proton potential of the deuteron (referred to as 2). These potentials have the form

$$V_i(r) = \begin{cases} -V_{0i}, & r < R_i \\ 0, & r > R_i \end{cases} \quad (i = 1,2), \tag{24}$$

where R_1 is the radius of the heavy nucleus and V_{01} is its potential depth. Similarly, R_2 is the radius of the deuteron and V_{02} is its potential depth. The distance r is the separation between the neutron and the center of the core of the heavy nucleus for the first system and in the second system it is between the neutron and proton in the deuteron.

Ignoring the nucleon's spin, let us consider the time-independent Schrödinger equation of only a single neutron in the potential given by Eq. (24) as

$$-\frac{\hbar^2}{2\mu_i}\nabla^2\phi_i(\vec{r}) + V_i(r)\phi_i(\vec{r}) = \mathcal{E}_{bi}\,\phi_i(\vec{r}), \quad (i = 1,2), \tag{25}$$

where $\mu_i = m_n M_i/(m_n + M_i)$ is the reduced mass, m_n is the neutron mass, M_i is the mass of the heavy nucleus (if $i = 1$) or the proton (if $i = 2$), and $\vec{r}$ is the relative position of the neutron with respect to the center of mass of the heavy nucleus ($i = 1$) or the proton ($i = 2$). As known from elementary

studies, the solution of the wave function for central potentials can be separated into radial and angular parts as $\phi_i(r) = R_{in\ell}(r)\,Y_{\ell m}(\theta,\phi)$. For the case of a ground- state solution ($n = 1$, $\ell = 0$), we substitute with the form $R_{in\ell}(r) = u_i(r)/r$ in Eq. (25) to obtain the acceptable solutions of $\phi_i(r)$ in the two regions of r as

$$\phi_i(r) = \begin{cases} A_i \dfrac{\sin(\kappa_i r)}{r}, & r \leqslant R_i \\ B_i \dfrac{e^{-k_i r}}{r}, & r \geqslant R_i \end{cases} \qquad (i = 1,2), \tag{26}$$

where κ_i, k_i, A_i, and B_i (with $i = 1, 2$) are given by

$$\kappa_i = \sqrt{\frac{2\mu_i(V_{0i} - |\mathcal{E}_{bi}|)}{\hbar^2}}, \quad k_i = \sqrt{\frac{2m_n|\mathcal{E}_{bi}|}{\hbar^2}},$$

$$A_i = \frac{1}{\sqrt{4\pi}}\sqrt{\frac{2k_i}{1+k_iR_i}}, \quad B_i = \frac{\sin(\kappa_i R_i)}{\sqrt{4\pi}}\sqrt{\frac{2k_i}{1+k_iR_i}}\,e^{k_iR_i}.$$

Finiteness of $\phi_i(r)$ and the continuity of $u_i(r)$ and $du_i(r)/dr$ leads to the transcendental equation

$$\cot\alpha_i = -\frac{k_i\,R_i}{\alpha_i}, \quad \text{where} \quad \alpha_i = \kappa_i R_i. \tag{27}$$

When assuming a spherical ^{156}Gd nucleus of radius $R_1 = r_o A^{1/3}$, with $r_o = 1.24$ fm, this choice gives $R_1 = 6.69$ fm, which is between the values of $(R_T)_{min}$ and $(R_T)_{max}$; see Fig. 4. With this model, it is proposed to search for a neutron energy level near the top of the potential well that matches the experimental neutron separation energy, $S_n = 8.536$ MeV [30]. Consequently, the variation of the depth V_{01} will lead to this energy level when solving the transcendental equation given by Eq. (27) and finding values of α_1 that result from the intersection of the two functions $\cot\alpha_1$ and $-k_1R_1/\alpha_1$. The nuclear potential depth $V_{01} = 48.718$ MeV produces this top energy level. This level has $\alpha_1 = 9.240$ rad and is categorized by the values $\kappa_1 = 1.388$ rad/fm and $k_1 = 0.640$ rad/fm.

The stable weakly bound deuteron that can be described by using Eq. (24) has a binding energy $\mathcal{E}_{b2} = 2.2245$ MeV and a matter radius $R_2 = 1.975$ fm. Using these two well-known values, we solve the transcendental equation, Eq. (27), and plot both the two functions $\cot\alpha_2$ and $-k_2R_2/\alpha_2$ versus α_2. The two functions intersect at one value $\alpha_2 = 1.817$ rad, which gives $V_{02} = 37.3$ MeV, $\kappa_2 = 0.92$ rad/fm, and $k_2 = 0.232$ rad/fm.

V. PICKUP OF A NEUTRON AT THE POINT OF CA IN A (p,d) REACTION

In the ^{156}Gd(p,d)^{155}Gd reaction, we study the interaction of a proton with the nucleus until it reaches the point of closest approach (CA). Then we consider the pickup of a loosely bound neutron at CA. This can be done if the ^{156}Gd nucleus is considered to consist of a ^{155}Gd nucleus core plus a valence neutron. This reaction is illustrated as:

$$\mathrm{p} + {}^{156}\mathrm{Gd} \xrightarrow[\text{near CA}]{} \mathrm{p} + (\mathrm{n} + {}^{155}\mathrm{Gd}) = \mathrm{d} + {}^{155}\mathrm{Gd} \tag{28}$$

Therefore, if we consider a quasi-break-up process, then away from the CA we deal only with a two-body problem as shown in Fig. 3, while near the CA, we deal with a three-body problem. We let $\vec{r}$ be the position of the proton with respect to the center of the nucleus.

To treat the interaction generally in the incoming channel for $r_{CA} \leqslant r < \infty$, we immediately see that the total Hamiltonian contains two interactions. The first interaction is determined by the Hamiltonian $H_p(\vec{r})$, which deals with the proton until a point near the CA and does not consider a neutron pickup. The real part of $H_p(\vec{r})$ governs the proton's motion; whereas the imaginary part represents the absorptive component and facilitates the absorption of protons and becomes effective in the vicinity of nuclear matter. Explicitly, this Hamiltonian contains the real and imaginary potentials given by Eq. (6), which includes the Coulomb potential, Eq. (7), plus the real and imaginary optical potentials, Eq. (8) and Eq. (9). Formally, we write

$$H_p(\vec{r}) = \frac{\hat{\vec{P}}_p^2}{2m_p} + V_{pT}^{C}(r) + V_{pT}^{Opt}\big(r, E_p^{lab}\big) + i\,W_{pT}^{Opt}\big(r, E_p^{lab}\big). \tag{29}$$

The time-dependent Schrödinger equation of the proton is

$$i\hbar\frac{\partial}{\partial t}\Psi_p(\vec{r},t) = H_p(\vec{r})\,\Psi_p(\vec{r},t). \tag{30}$$

The technique of separation of variables allows us to have

$$\Psi_p(\vec{r},t) = \chi_p(t)\,\phi_p(\vec{r}). \tag{31}$$

We make the ansatz solutions of the wave function $\phi_p(\vec{r})$ and $\chi_p(t)$ as follows:

$$\left[\frac{\hat{\vec{P}}_p^2}{2m_p} + V_{pT}^{C}(r) + V_{pT}^{Opt}\big(r, E_p^{lab}\big)\right]\phi_p(\vec{r}) = E\phi_p(\vec{r}), \tag{32}$$

$$\chi_p(t) = a_p(t)\,\mathrm{e}^{-i\,E\,t/\hbar}, \tag{33}$$

where $E \equiv E_{pT}^{c.m.}$ is the proton's c.m. energy and $a_p(t)$ is the probability amplitude at time t that the proton has not been absorbed by the imaginary optical potential. Initially, at $t = 0$, when $r = \infty$, we must have $a_p(0) = 1$ since the imaginary optical potential is zero at infinity.

A. Probability of a surviving proton near CA

Equation (32) is very difficult to solve due to the complicated form of the optical potential. Instead, we use the results of the classical trajectories presented in Sec. III, specifically the variation of r with time t. When substituting from Eq. (31) into Eq. (30), with $\chi_p(t)$ given by Eq. (33), and then employing Eq. (32), we get

$$i\hbar\frac{d}{d\,t}a_p(t) = i\,a_p(t)\,W_{pT}^{Opt}\big(r, E_p^{lab}\big). \tag{34}$$

Figure 8 shows the variation of $W \equiv W_{pT}^{Opt}$ and $W \equiv W_{oR}^{Opt}$.

Integrating Eq. (34) from $t = 0$ to $t = t_{CA}$ and then to any value t will give the probability amplitude that the proton would survive being absorbed until time t. Thus,

$$a_p(t) = \exp\left[\hbar^{-1}\int_0^t W_{pT}^{Opt}\big(r(t), E_p^{lab}\big)\,dt\right], 0 \leqslant t \leqslant \infty. \tag{35}$$

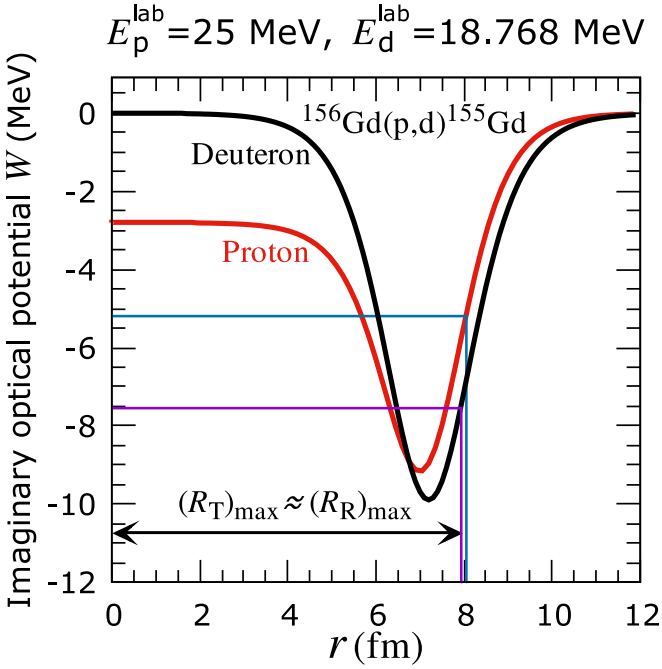

FIG. 8. For $0 < r \leqslant 12$ fm, the negative values of the imaginary optical potential W are displayed for protons (red), Eq. (9), and with similar equation for the deuteron (black) [26].

For $b_p = 7.230175$ fm, Fig. 9 displays the variation of $r(t)$, $W_{pT}^{Opt}(r(t), E_p^{lab})$, the integration in Eq. (35), and the survival probability of protons $|a_p(t)|^2$ with respect to t (in yocto seconds, 1 ys $= 10^{-24}$ s) and in a region where $W \neq 0$.

An offset of 149,236 ys is taken to correspond the zero time in Fig. 9. This represents the elapsed time from $t = 0$ until $W_{pT}^{Opt}(r(t), E_p^{lab}) \simeq 0$. At CA we have t_{CA}=734.4 ys, $r_{CA} =$ 8.98 fm, $W_{pT}^{Opt} = -1.59$ MeV, $\int_0^{t_{CA}} W_{pT}^{Opt} dt = -98.5$ MeV $\cdot$ ys, and a probability of about 74.1 % that the proton would survive absorption by the imaginary optical potential. At infinity, the probability decreases to about 55 %.

B. Probability of neutron transfer near CA

The second important interaction in the incoming channel for $r_{CA} \leqslant r < \infty$ is near the target nuclear matter and particularly near the CA. This interaction describes the possible transfer of a loosely bound neutron from the heavy nucleus to the proton, forming a deuteron.

With respect to the arbitrary origin o and at a time t, we let $\vec{r}_1$ and $\vec{r}_2$ be the c.m. positions of the target and proton, respectively, see Fig. 10. In this figure, $\vec{r}$ and $\vec{r}_n$ are the positions of the proton with respect to the target nucleus and neutron with respect to o, respectively. If we take o at the center of the target, then $\vec{r}_1 = 0$ and $\vec{r}_2 = \vec{r}$.

The total Hamiltonian of the system can be written as

$$H(\vec{r},\vec{r}_n) = H_p(\vec{r}) + H_n(\vec{r}_n,\vec{r}), \tag{36}$$

and this satisfies the time-dependent Schrödinger equation:

$$i\hbar \frac{\partial}{\partial t}\Psi(\vec{r},\vec{r}_n,t) = [H_p(\vec{r}) + H_n(\vec{r}_n,\vec{r})]\,\Psi(\vec{r},\vec{r}_n,t), \tag{37}$$

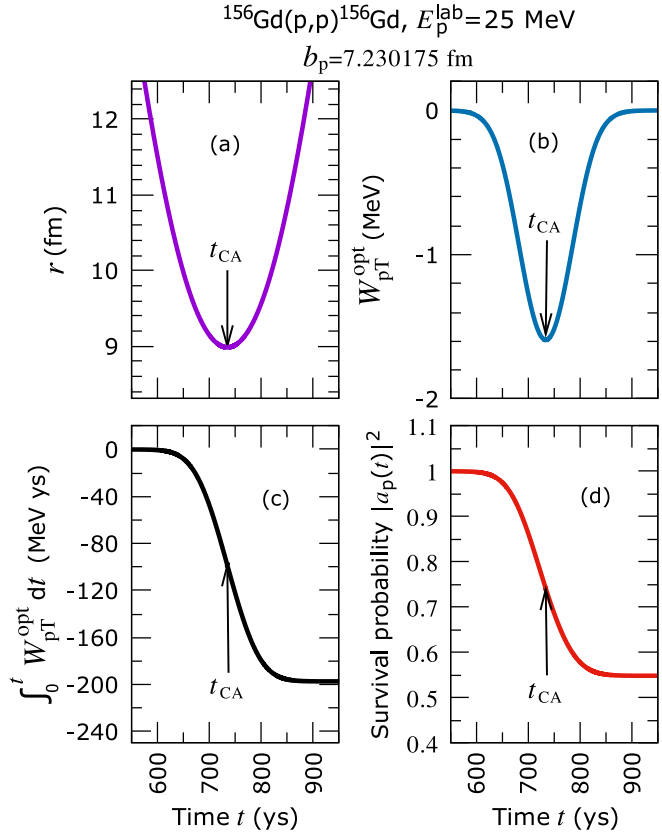

FIG. 9. Variation with time t when 550 ys $\leqslant t \leqslant$ 950 ys for (a) r, (b) W_{pT}^{Opt}, (c) $\int_0^t W_{pT}^{Opt} dt$, and (d) $|a_p(t)|^2$. For the regions $t <$ 630 ys and $t >$ 875 ys, almost no proton absorption occurs.

where the total wave function $\Psi(\vec{r},\vec{r}_n,t)$ is the product of the proton and neutron wave functions:

$$\Psi(\vec{r},\vec{r}_n,t) = \Psi_p(\vec{r},t)\,\Psi_n(\vec{r}_n,t). \tag{38}$$

The Hamiltonian of the neutron in the region of the closest approach can considered as

$$H_n(\vec{r}_n,\vec{r}) = \frac{\hat{\vec{P}}_n^2}{2m_n} + V_1(|\vec{r}_n - \vec{r}_1|) + V_2(|\vec{r}_n - \vec{r}_2|), \tag{39}$$

where m_n is the mass of neutron. We assumed that $V_1(|\vec{r}_n - \vec{r}_1|)$ is the real potential felt by the neutron when it interacts with the target nucleus. Similarly, $V_2(|\vec{r}_n - \vec{r}_2|)$ is real potential when it interacts with the proton. Consequently, the time-dependent Schrödinger equation that describes the neutron is

$$i\hbar \frac{\partial \Psi_n(\vec{r}_n,t)}{\partial t} = \left[\frac{\hat{\vec{P}}_n^2}{2m_n} + V_1(|\vec{r}_n - \vec{r}_1|) + V_2(|\vec{r}_n - \vec{r}_2|)\right]\Psi_n(\vec{r}_n,t). \tag{40}$$

It is possible to separate the variables in $\Psi_n(\vec{r}_n,t)$ as a product of space and time functions. For the space-dependence part, we denote $\phi_1(|\vec{r}_n - \vec{r}_1|)$ to be the neutron real wave function in the target nucleus, and we denote $\phi_2(|\vec{r}_n - \vec{r}_2|)$ to be the neutron wave function in the deuteron. The two wave functions ϕ_i, $(i = 1,2)$ are assumed to satisfy the Schrödinger

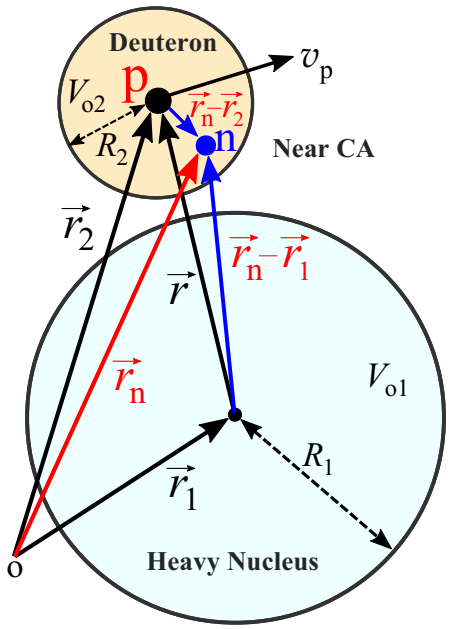

FIG. 10. At time t near the point of CA, and with respect to an arbitrary origin o, the positions of the proton and the loosely- bound neutron are $\vec{r}_2$ and $\vec{r}_n$, respectively. The figure displays an exaggerated deuteron size.

equations:

$$\left[\frac{\hat{\vec{P}}_n^2}{2m_n}+V_i(|\vec{r}_n-\vec{r}_i|)\right]\phi_i(|\vec{r}_n-\vec{r}_i|)=\boldsymbol{\mathcal{E}}_i\,\phi_i(|\vec{r}_n-\vec{r}_i|), \quad (41)$$

where $\boldsymbol{\mathcal{E}}_1$ and $\boldsymbol{\mathcal{E}}_2$ are the binding energies of the neutron in the heavy nucleus and deuteron, respectively. In Eq. (41), the reduced masses are not used because we are taking the c.m. vectors $\vec{r}_1$ and $\vec{r}_2$ as being fixed in space at time t and also we are also neglecting the recoil effects.

Based on the proposed approximate spherical square-well potential given by Eq. (24), the two forms displayed in Eq. (26) are based on an origin at the center of the heavy nucleus. These two forms can be modified to consider the origin o shown in Fig. 10. Therefore, expressions of $\phi_i(|\vec{r}_n-\vec{r}_i|)$ can be written as

$$\phi_i(|\vec{r}_n-\vec{r}_i|)=\begin{cases}A_i\,\dfrac{\sin\kappa_i\ |\vec{r}_n-\vec{r}_i|}{|\vec{r}_n-\vec{r}_i|}, & |\vec{r}_n-\vec{r}_i|\leqslant R_i\\[2ex] B_i\,\dfrac{e^{-k_i|\vec{r}_n-\vec{r}_i|}}{|\vec{r}_n-\vec{r}_i|}, & |\vec{r}_n-\vec{r}_i|\geqslant R_i\end{cases}. \quad (42)$$

For the time dependence part of $\Psi_n(\vec{r}_n,t)$, we separate the position dependence in $\vec{r}_n$ and time t by

$$\Psi_n(\vec{r}_n,t)=\chi_1'(t)\,\phi_1(|\vec{r}_n-\vec{r}_1|)+\chi_2'(t)\,\phi_2(|\vec{r}_n-\vec{r}_2|). \quad (43)$$

The separation of variables technique will allow us to write the time-dependent function $\chi_n'(t)$ as

$$\chi_n'(t)=a_n'(t)\,e^{-i\,\boldsymbol{\mathcal{E}}_n\,t/\hbar}, \quad (n=1,2), \quad (44)$$

where $a_1'(t)$ is the probability amplitude at time t of a neutron being in the heavy nucleus and $a_2'(t)$ is that at the same time for being picked up by the proton. Initially, at $t=0$, we have $a_1'(t=0)=1$ and $a_2'(t=0)=0$. Moreover, $a_1'(t=t_{CA})$ is the probability amplitude at CA when the neutron stays in the target nucleus, while $a_2'(t=t_{CA})$ is that when the neutron is captured by the proton at CA.

Substituting with $\Psi_p(\vec{r},t)$, given by Eq. (31), and $\Psi_n(\vec{r}_n,t)$, given by Eq. (43), into Eq. (38) we get the following total wave function of the system:

$$\Psi(\vec{r},\vec{r}_n,t)=[\chi_1(t)\,\phi_1(|\vec{r}_n-\vec{r}_1|)+\chi_2(t)\,\phi_2(|\vec{r}_n-\vec{r}_2|)]\times\phi_p(\vec{r}), \quad (45)$$

where $\chi_1(t)=\chi_1'(t)\chi_p(t)$ and $\chi_2(t)=\chi_2'(t)\chi_p(t)$. From Eqs. (44) and (33) we have

$$\chi_n(t)=a_n(t)\,e^{-i\,(\boldsymbol{\mathcal{E}}_n+E)\,t/\hbar}, \quad (n=1,2), \quad (46)$$

where $a_n(t)=a_n'(t)\,a_p(t),(n=1,2)$. Now, $a_1(t)$ is the probability amplitude, at time t, a neutron that has not been picked up by a proton which has not been absorbed by the imaginary optical potential. Initially, at $t=0$, we have $a_1(0)=a_1'(0)\,a_p(0)=1$. Additionally, $a_2(t)$ is the probability amplitude, at time t, a neutron that is being picked up by a proton which has not being absorbed by the imaginary part of the optical potential. Initially, $a_2(0)=a_2'(0)\,a_p(0)=0$ at $t=0$. Likewise, $a_2(t_{CA})$ is the probability amplitude at the CA of picking up a neutron by a surviving proton.

Substituting Eq. (45) into Eq. (37), and after some algebra, we arrive to the following differential equation:

$$\dot{a}_n(t)=\frac{1}{i\,\hbar}\left[(X_{n\,m}+i\,W)\,a_n(t)+Y_{n\,m}e^{-i\,\frac{(\boldsymbol{\mathcal{E}}_m-\boldsymbol{\mathcal{E}}_n)\,t}{\hbar}}a_m(t)\right], \quad (47)$$

where $W\equiv W_{pT}^{Opt}$,

$$X_{n\,m}=\frac{\langle nmn\rangle-\langle 12\rangle\langle nmm\rangle]}{1-\langle 12\rangle^2},\qquad Y_{n\,m}=\frac{\langle nnm\rangle-\langle 12\rangle\langle mnm\rangle}{1-\langle 12\rangle^2},\qquad \begin{cases}n=1,m=2\\ \text{or}\\ n=2,m=1\end{cases}, \quad (48)$$

and we used the bra-ket notation to represent the resulting overlap integrals shown in Table V.

In all overlap integrals, $\phi_i(|\vec{r}_n-\vec{r}_i|)$ of Eq. (42) is used to find $X_{n\,m}$ and $Y_{n\,m}$ analytically. For convenience we use the dimensionless parameters $\alpha_{ij}=k_iR_j$, $\beta_i=k_ir_{12}$, $\gamma_i=\kappa_iR_i$, $\delta_i=\kappa_ir_{12}$, and $F_i=R_i/r_{12}$, where if $i=1$ then $j=2$ or if $i=2$ then $j=1$. The analytical expressions of $\langle 121\rangle$ and

TABLE V. Shorthand symbols for the bra-ket notation.

Overlap integral	Shorthand symbol
$\langle\phi_1\|V_2\|\phi_1\rangle$	$\langle 121\rangle$
$\langle\phi_2\|V_1\,\|\phi_2\rangle$	$\langle 212\rangle$
$\langle\phi_2\|V_2\|\phi_1\rangle=\langle\phi_1\|V_2\|\phi_2\rangle$	$\langle 221\rangle=\langle 122\rangle$
$\langle\phi_1\|V_1\,\|\phi_2\rangle=\langle\phi_2\|V_1\,\|\phi_1\rangle$	$\langle 112\rangle=\langle 211\rangle$
$\langle\phi_1\|\phi_2\rangle=\langle\phi_2\|\phi_1\rangle$	$\langle 12\rangle=\langle 21\rangle$

$\langle 212\rangle$ are evaluated and combined as

$$\langle iji\rangle = \frac{V_{0j}\,\beta_i \sin^2(\gamma_i)\, e^{2\alpha_{ii}}}{(1+\alpha_{ii})}\left[F_j - \left(1-F_j^2\right)\ln\frac{1+F_j}{1-F_j} + 2\sum_{n=1}^{\infty}\sum_{\ell=1,3,..}^{n}\frac{(-2\beta_i)^n F_j^{\ell+2}}{n\,(n-\ell)!\,\ell!\,(\ell+2)}\right], \begin{cases} i=1, j=2 \\ \text{or} \\ i=2, j=1 \end{cases}, \tag{49}$$

where the summation term converges rapidly after about reaching 30 to 50 terms. The analytical expressions of $\langle 112\rangle$ and $\langle 122\rangle$ can take the following combined form (with the alteration of i and j as defined previously):

$$\langle 1\,i\,2\rangle = \frac{2V_{0i}\,\sin\gamma_j\; e^{\alpha_{jj}-\beta_j}}{\sqrt{(1+\alpha_{11})(1+\alpha_{22})}\left(\delta_i^2+\beta_j^2\right)}\sqrt{\frac{\beta_i}{\beta_j}} \times [\beta_j \sin\gamma_i\;\cosh\alpha_{ji} - \delta_i\cos\gamma_i\;\sinh\alpha_{ji}]. \tag{50}$$

The analytical integration of $\langle\phi_1|\,\phi_2\rangle$ is divided into three parts. The first part is carried out when the neutron of Fig. 10 lies inside the *heavy nucleus* domain. The domain of the second part is taken when the neutron lies inside the *deuteron*. The integration of the third part is carried out when the neutron is outside both the *heavy nucleus* and the *deuteron*. By taking the origin in Fig. 10 in this case at the heavy nucleus, we allow $\vec{r}_{\rm n}$ to cover the whole domain D given by $R_1 \leqslant r_{\rm n} \leqslant \infty, 0 \leqslant \theta \leqslant \pi$, and $0 \leqslant \phi \leqslant 2\pi$ even when $|\vec{r}_{\rm n} - \vec{r}| < R_2$. Of course, this domain D will cover the unwanted region of the deuteron. Since the size of the deuteron is negligible with respect to the huge domain D, this choice of integration is perfectly valid. Accordingly, the analytical integration of $\langle\phi_1|\,\phi_2\rangle = \langle 12\rangle$ will be

$$\begin{aligned}\langle 12\rangle = \frac{2}{\sqrt{(1+\alpha_{11})(1+\alpha_{22})}}\Bigg[&\sqrt{\frac{\beta_1}{\beta_2}}\frac{\sin\gamma_2\; e^{\alpha_{22}-\beta_2}}{\left(\beta_2^2+\delta_1^2\right)} \times \{\beta_2\sin\gamma_1\;\cosh\alpha_{21} - \delta_1\cos\gamma_1\;\sinh\alpha_{21}\} \\ &+\sqrt{\frac{\beta_2}{\beta_1}}\frac{\sin\gamma_1\; e^{\alpha_{11}-\beta_1}}{\left(\beta_1^2+\delta_2^2\right)} \times \{\beta_1\sin\gamma_2\;\cosh\alpha_{12} - \delta_2\cos\gamma_2\;\sinh\alpha_{12}\} \\ &+\sqrt{\frac{\beta_1}{\beta_2}}\frac{\sin\gamma_1\sin\gamma_2 e^{\alpha_{11}+\alpha_{22}}}{(\beta_1+\beta_2)}\Bigg\{e^{-\beta_1-\beta_2}\sinh\beta_2 \\ &+\frac{e^{-\beta_2}}{(\beta_1-\beta_2)}[e^{-\alpha_{11}}(\beta_1\sinh\alpha_{21}+\beta_2\cosh\alpha_{21}) \\ &-e^{-\beta_1}(\beta_1\sinh\beta_2+\beta_2\cosh\beta_2)]\Bigg\}\Bigg].\end{aligned} \tag{51}$$

We now turn back to the coupled-first-order linear differential equations, Eq. (47). We can write them as

$$\begin{aligned}\dot{a}_1(t) &= g_{11}\,a_1(t) + g_{12}\,e^{-i\omega t}a_2(t), \\ \dot{a}_2(t) &= g_{21}\,e^{+i\omega t}a_1(t) + g_{22}\,a_2(t),\end{aligned} \tag{52}$$

where $\omega = \boldsymbol{\mathcal{E}}_{21}/\hbar = (\boldsymbol{\mathcal{E}}_2 - \boldsymbol{\mathcal{E}}_1)/\hbar$. The g's are related to the coefficients X_{nm}, Y_{nm}, and the imaginary optical potential W by the following relations:

$$\begin{aligned} g_{11} &= (i\hbar)^{-1}(X_{12}+iW), \quad g_{12} = (i\hbar)^{-1}Y_{12}, \\ g_{21} &= (i\hbar)^{-1}Y_{21}, \quad g_{22} = (i\hbar)^{-1}(X_{21}+iW).\end{aligned} \tag{53}$$

We cannot solve these coupled-first-order differential equations using the normal procedure of matrix algebra since some coefficients are time-dependent. When using the technique of the Laplace transform, we can find the probability at time $0 \leqslant t \leqslant t_{\rm CA}$ of picking-up a neutron by a surviving proton as

$$|a_2(t)|^2 = 1 - e^{2Wt/\hbar}\,[1 - C\sin^2(ft)], \quad 0 \leqslant t \leqslant t_{\rm CA}, \tag{54}$$

where due to the negative values of the imaginary optical potential W (see Fig. 8), the attenuation factor $e^{2Wt/\hbar}$ goes from 1 to a smaller value $e^{2Wt_{\rm CA}/\hbar}$ when t goes from 0 to $t_{\rm AC}$. The values of f and the factor C in Eq. (54) are related to the predefined coefficients and are given by

$$\begin{aligned} f^2 &= A^2 + B^2, \quad A = \tfrac{1}{2}\hbar^{-1}(\boldsymbol{\mathcal{E}}_{21} + X_{21} + X_{12}), \\ B &= \hbar^{-1}[\boldsymbol{\mathcal{E}}_{21}X_{12} + X_{12}X_{21} - Y_{12}Y_{21}]^{1/2}, \\ C &= 1 - D^2/f^2, \quad D = \tfrac{1}{2}\hbar^{-1}(\boldsymbol{\mathcal{E}}_{21} + X_{21} - X_{12}).\end{aligned} \tag{55}$$

The numerical values of f and D are very close to each other (usually of the order of $4\times10^{-3}\,(\text{ys})^{-1}$ for most of the impact parameters in this study). Therefore, C has a very small value or zero. In addition, even with the violent fluctuation of $\sin^2(ft)$ in the time scale of $t > 530$ ys, we end up with a simpler probability formula (with a second term that is similar to the well-known WKB penetration probability) for picking-up a neutron by a survived proton:

$$|a_2(t)|^2 \simeq 1 - e^{2Wt/\hbar}, \quad 0 \leqslant t \leqslant t_{\rm CA}. \tag{56}$$

Similar steps to Eq. (29) through Eq. (34) can be applied to the deuteron after the CA. These steps will give the probability amplitude, $a_{\rm d}(t)$, that the deuteron would survive from being absorbed by the deuteron optical potential an any time $t \geqslant t_{\rm CA}$. Therefore,

$$a_{\rm d}(t) = \exp\left[\hbar^{-1}\int_{t_{\rm CA}}^{\infty} W_{\rm dR}^{\rm Opt}\left(r(t), E_{\rm d}^{\rm lab}\right)\,dt\right]. \tag{57}$$

For the incoming channel ($t \leqslant t_{\rm CA}$) and for three different impact parameters, the left rising part of Fig. 11 displays $|a_2(t)|^2$ as a function of time t (in ys), when using the same offset time 149,236 ys as in Fig. 9. All trajectories start at $t = 0$ when the distance D in Fig. 3 is about 10^4fm. For the smallest selected value, $b_{\rm p} = 7.23$ fm, Fig. 11 indicates that the probability starts to increase gradually after $t \approx 600$ ys. The probability that a surviving proton can pick up a neutron and form a deuteron is about 38.6% at CA when the proton reaches $r_{\rm CA} = 8.98$ fm at $t_{\rm CA} \simeq 734$ ys. For the selected value, $b_{\rm p} = 7.60$ fm, the bottom blue curve of the figure shows the same trend of increase. The probability of forming a deuteron is about 16% when the proton reaches $r_{\rm CA} \simeq 9.50$ fm at $t_{\rm CA} \simeq 720$ ys. Thus, for large impact parameters, the chance of forming a deuteron near the CA decreases as expected.

For the outgoing channel ($t \geqslant t_{\rm CA}$), the attenuated right part of the same figure displays $|a_{\rm d}(t)|^2$ as a function of time for

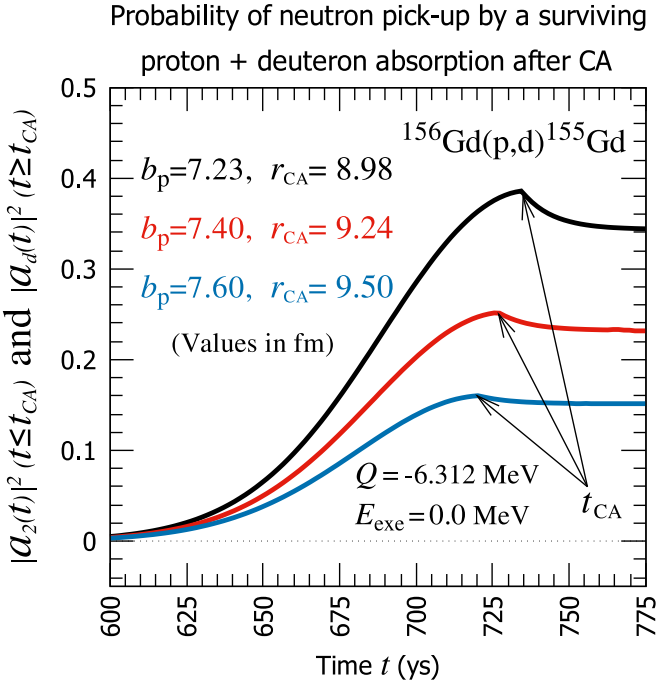

FIG. 11. Graph of the variation of $|a_2(t)|^2$,$(0 \leqslant t \leqslant t_{CA})$ and $a_d(t)$, $(t \geqslant t_{CA})$ for three selected impact parameters.

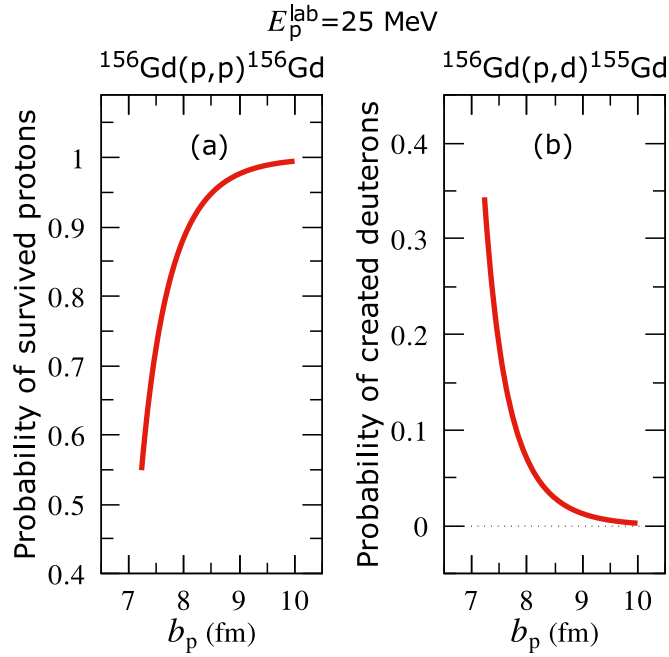

FIG. 12. The survival probability as a function of the impact parameter is plotted for protons (a) and deuterons (b).

t (in ys). For the small value $b_p = 7.23$ fm, Fig 11 indicates that the deuteron imaginary optical potential has considerable effect on absorbing the deuterons. As a comparison, this effect goes away much less than the absorption that occurs for the case of the proton, as seen in Fig. 9. The probability of creating a deuteron drops from 38.6% at CA to only 34.4% when detected at infinity. The figure indicates that larger impact parameters have a limited effect on absorbing deuterons after their formation at CA. In other words, the absorption effect on the formed deuterons is not appreciable when the protons have relatively large impact parameters.

C. Angular distribution weighted by probability

Based on the formulations of the subsections A and B, we calculated 276,983 weighted trajectories for protons and a similar number of deuterons created at CA. Figure 12(a) shows the probability that a proton was not absorbed by the imaginary optical potential as a function of the impact parameter. Since deuterons can be created in the forward direction only when $b_p \geqslant 7.23018$ fm, this part of the figure starts with the proton probability loss of 0.55 when detected. As b_p increases, the survival probability increases and reaches a value close to 1 when $b_p = 10$ fm (no proton loss).

Figure 12(b) shows the probability of a neutron that is picked up by a proton which is not absorbed by the imaginary optical potential, and hence forming a deuteron. At $b_p = 7.23487$ fm, the probability of creating a deuteron at CA and then detected at infinity is 0.35. As b_p increases, the deuteron's probability decreases and when $b_p = 10$ fm, it reaches a very small value of 0.003.

Figure 13(a) displays the number of detected protons at infinity, N_p, weighted by their survival probability as a function of θ_p (with a bin size $\Delta\theta_p = 1.5^\circ$). Here one can see a smooth gradual increase followed by a sharp increase in the number

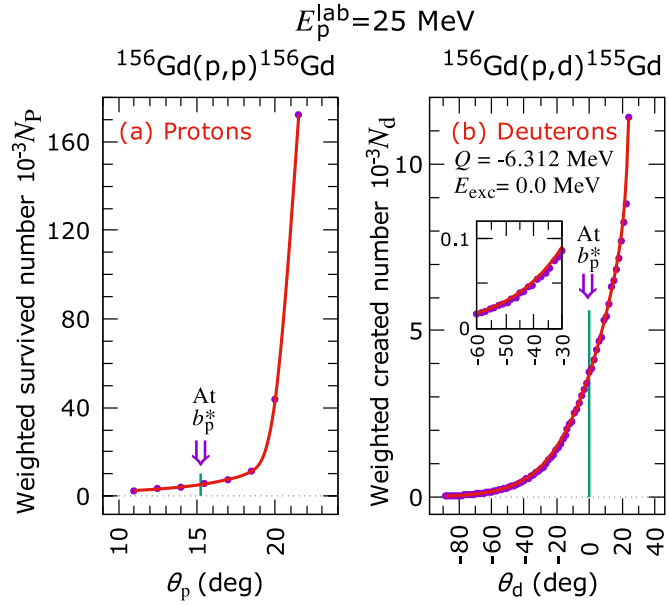

FIG. 13. Each point on the abscissa represents a bin size of $\Delta\theta_p = \Delta\theta_d = 1.5^\circ$. (a) Angular distribution weighted by a proton's survival probability. (b) The same as (a), but for deuterons weighted by their creation probability at CA and then surviving from being absorbed by the imaginary optical potential after the CA and then detected. A smaller window is added to show the number of deuterons in the experimental range.

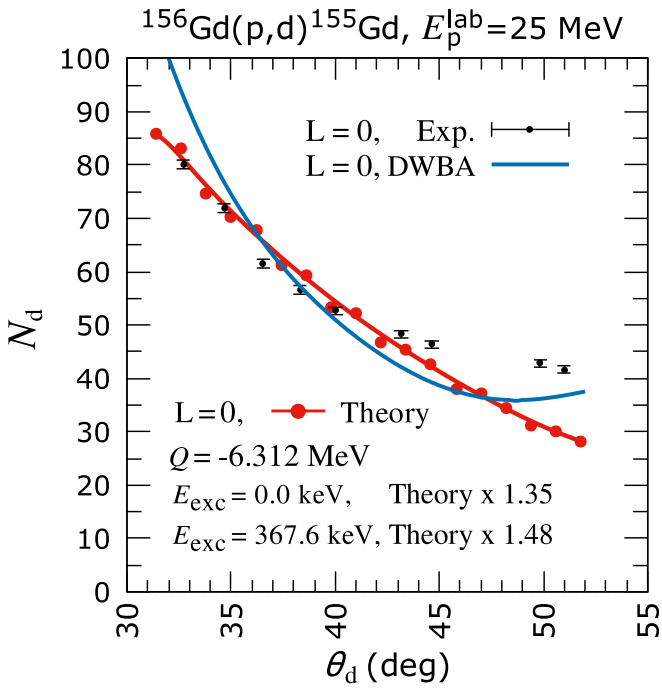

FIG. 14. Comparison between the deuterons angular distributions of the present calculations with the experimental angular momentum transfer L = 0 data for the direct population of the ground state and the level 367-keV, $\frac{1}{2}^+$[400] of Allmond *et al.* [10] and L = 0 DWBA calculations [11].

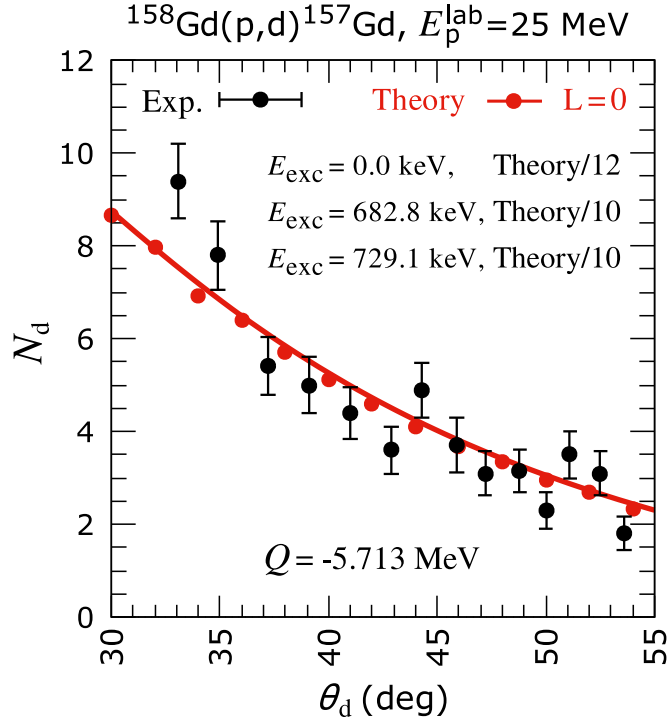

FIG. 15. Comparison between the experimental results of T. Ross *et al.* [4] and the present calculations for deuterons.

of protons. The change in angles occurs in the range $11^\circ \lesssim \theta_p \lesssim 21.5^\circ$ with the number of protons in the range $2 \lesssim N_p \lesssim 173{,}000$.

Figure 13(b) displays, as a function of θ_d (with a bin size $\Delta\theta_d = 1.5^\circ$), the number of detected deuterons N_d, weighted by their probability (after the creation at CA and detected at infinity). The number of deuterons becomes significant after $\theta_d > -70^\circ$ and increases gradually in the beginning and then violently to a peak at about $\theta_d \simeq 25^\circ$ when $N_d \simeq 11{,}500$. The trajectory calculations show that when $b_p^* = 7.40091$ fm we get final angles $\theta_p \simeq 15.215^\circ$ and $\theta_d = 0^\circ$. This is indicated by the two arrows in both parts of Fig. 13. For values greater than b_p^*, θ_d is positive and reaches a maximum at $\theta_d \simeq 25^\circ$.

As displayed in both the top and bottom parts of Fig. 2, the observed experimental results are for angles greater than 30° and less than 60° [10,4]. Therefore, we need to plot the calculated theoretical number N_d for only the angles in Fig. 13(b) that fall within the experimental measurements.

To get a good fit with the experimental results, the calculated values for the ground state of ^{155}Gd in Fig. 13(b) are scaled up by a factor of 1.35 and plotted in Fig. 14. To get the curve of the 367.6 keV level to overlap with the ground-state curve of Fig. 14, a scaling-up factor of 1.48 is used. This indicates that, for the excited ^{155}Gd nucleus, the number of detected deuterons is smaller. Thus, exciting ^{155}Gd nucleus to higher Nilsson levels contributes fewer detected deuterons than that with the ground energy.

As seen from Fig. 14, our theory fits the experimental values for all small angles except at the two large angles 49.84° and 50.99°. The overall fit looks acceptable and describes the general features of the experimental results, even without considering the interference between deuterons created with negative and positive angles. This is because positive angles have a maximum value of about $\theta_d = 25^\circ$; see Fig. 13(b). Therefore, deuterons with positive angles are considered to be in the direction of the proton's beam. The L = 0 DWBA curve displayed in Fig. 14 passes through the experimental curve at 38.31° and deviates most from the experiment at small and large angles.

According to the CCBA theory presented by Ascuitto and Glendenning for the stripping (d,p) reaction [31] and the two-neutron transfer (p,t) reaction [32], there are certain situations where one or two of the usual three assumptions for the DWBA are false when considering transfer reactions. This might explain why the DWBA cannot explain the experimental results of Fig. 14. On the other hand, the CCBA theory is more complex in its formalism than our simple semi-classical approach, which gives a reasonable fit to the experiment. Unfortunately, no published research literature relevant to CCBA is available in the case of 25 MeV proton incident on ^{156}Gd nucleus in a (p,d) reaction.

Following the DWBA angular-distribution fit which is best characterized by angular momentum transfer L = 0,1,2 for the experimental work of Ref. [4], Fig. 15 shows the calculations for the ^{158}Gd(p,d)^{157}Gd reaction when considering the ground state and the two states shown in Table VI.

In Fig. 15 we compare the results of our angular momentum transfer L = 0 theory with experimental work of T. Ross *et al.* [4]. To get a good fit with the experimental work, the calculated values for the ground state are scaled down by a factor of 1/12.

TABLE VI. Experimental energy level of ^{157}Gd. Taken from Table 6 of Ref. [33].

E^*(keV)	J^π	$K[Nn_z\Lambda]$
682.84 (3)	$\frac{1}{2}^+$	$\frac{1}{2}$[400]
729.14 (3)	$\frac{3}{2}^-$	$\frac{1}{2}$[521]

To get the curves of the 682.84 and 729.14 keV levels to overlap with the ground state curve, a scaling-down factor of 1/10 is used.

Although the experimental work of Ross *et al.* [4] is not for L = 0, the semiclassical calculations agree with almost the highest 12 experimental angles and deviate in case of the two smallest angles.

For the comparison with the DWBA curves presented at 729 keV in Fig. 7 of Ref. [4] and displayed in the bottom of Fig. 2 of this paper, we note that the L = 0 DWBA curve does not fit the experiment and the L = 1,4 curves fit the data for angles less than 45° but deviate for angles greater than 45°. The comparison and agreement of our angular distribution with the experimental data presented in the bottom part of Fig. 2, which displayed in Fig. 15, is only for deflections greater than 30°. The DWBA curve does not show L = 0 at smaller angles, but it looks as if it could be extrapolated up at smaller angles. We might hope that experimental data could be extended into smaller angles, despite interference from elastically scattered protons. Again, the discrepancy between experiment and DWBA may be due to the strong coupling of inelastic channels to the ground in deformed nuclei, as indicated by the CCBA theory [31].

VI. RESULTS AND DISCUSSION

Using the optical model parameters of C. Perey and F. Perey [26], we see that the p,d pickup reaction must take place near the nuclear surface at the poles. That condition favors filled neutron orbitals with relatively large wave functions with $\Lambda = 0$, which guarantees a finite neutron population at the nuclear poles. Due to conservation of energy, the pickup will favor filled orbitals below the Fermi surface near the 2.2245 MeV binding energy of the final state deuteron. The most strongly populated final state in both p,d products of ^{155}Gd and ^{157}Gd is the $\frac{1}{2}^+$[400] state at 367.6 keV in ^{155}Gd and 682.8 keV in ^{157}Gd, which are a mix of $s_{1/2}$ and $d_{3/2}$ from the shell below N = 82 (see Table 11 from Ref. [1]). The fact that this dominant band has by far predominant population in its spin $\frac{1}{2}$ ground state, is a consequence of Coulomb excitation on the inward path of the proton being cancelled by that on the outward path of the formed deuteron. This is more evidence that most of the p,d pickup takes place near the poles.

One feature of the nuclear structure that has not been taken into account by Ross *et al.* [2] is the feature of "quadrupole pairing," Chu *et al.* [6]. This feature proved to be a major factor in accounting for the low energy of the first-excited 0^+ state in ^{154}Gd. We note that Chu's work [6] recognized that monopole pairing for solving the BCS-mixing equations needs special treatment in systems where the Nilsson orbitals divide into two groups: down-going and up-going. The former involves the nucleon wave functions that mainly occupy the north and south polar regions, whereas the up-going orbitals mainly occupy the equatorial regions. An exception to this general rule are the two most heavily populated bands in the p,d reaction, namely, the $\frac{1}{2}^+$[400] and the $\frac{3}{2}^+$[402]. From the weak signature splitting in these bands we know that there is considerable mixing of the s1/2 and d3/2 orbitals. Thus, they both have amplitudes at the nuclear poles from the presence of the s1/2 orbital. Both of these Nilsson states are available for neutron pickup at their poles, though the $\frac{1}{2}^+$[400] is the greater at the poles.

In systems with BCS mixing, transition rates have a uv factor. In the case of the odd-A Gd the up-going orbitals from the shell below the 82 gap are mostly filled with neutrons and v_n is near 1. For the orbitals near the Fermi energy most are downsloping (polar) and their BCS solution will have u (emptiness) and v (fullness) values of near square roots of $\frac{1}{2}$. This pairing influence gives an enhancement to pick up from the up-going orbitals well below the Fermi energy, such as $\frac{1}{2}^+$[400] and $\frac{3}{2}^+$[402]. That is, the removal of a neutron from the upgoing neutron-orbital will barely affect the BCS solution for the down-going orbitals.

Both bands ($\frac{1}{2}^+$[400] and $\frac{3}{2}^+$[402]) have the feature of a strong lobe in the wave function at the poles of the spheroid. This justifies our classical trajectories grazing the poles at 0 and 180 degrees latitude. Of more importance is that the proton beam energy, 25 MeV, was chosen for the maximum pickup probability by DWBA theoretical calculations. We understand that at lower beam energies, the protons are below the Coulomb barrier at all latitudes. The lowest Coulomb barrier is at the poles, where most of the p,d pickup occurs. The decline of the pickup cross section in DWBA at higher energies may be attributed to the increasing speed of the grazing protons at the poles.

One concern in our theoretical trajectory work is that we have used the Perey and Perey [26] optical-model parameters, which are based on a uniform spherical charge distribution. More recent parameters, such as the global optical potential [34,35] can also be used, but they have the same spherical charge distribution feature. The actual radius of curvature at the poles should be somewhat smaller than at the spherical nuclei, and the Coulomb potential will differ slightly due to the deformed nucleus. The refinement of the code to nonspherical shapes is a future challenge.

VII. CONCLUSIONS

We believe these semiclassical calculations for the dominant $\frac{1}{2}^+$[400] give a reasonable fit to experimental p,d angular distributions, which have only been measurable at angles larger than about 30 degrees, since smaller angles are flooded with scattered protons. The simple support for this conclusion is that the $\frac{1}{2}^+$[400] and $\frac{3}{2}^+$[402] are the most strongly populated states because they have the largest $C^2_{j\ell}$ coefficients for L = 0

and 2, respectively, and the kinematics are such that the cross sections are largest at these angles for $L = 0 - 2$.

Additionally, we believe that when the incoming proton wavelength is considerably smaller than the nuclear size, then this simplistic semi-classical code achieves a comparable fit with experimental results for the case of the angular momentum transfer $L = 0$ as compared to the DWBA approach used by the standard codes [11–14]. Also, since the presented approach is particularly suited for describing the angular momentum transfer $L = 0$, then it may provide an elegant framework for future investigations of excited 0^+ states populated in: (a) the (p,t) reaction [2,4,36–42]; (b) the (t,p) reaction [43,44]; (c) the (d,p) reaction [45]; and (d) the more heavier projectile reaction such as (^{3}He,α) [46–51].

ACKNOWLEDGMENTS

We thank James M. Allmond for providing us with the experimental data of the ^{156}Gd target and fruitful discussions about the experimental analysis of the ^{156}Gd(p,d)^{155}Gd. This work is partially supported by U.S. Department of Energy Grants and Contracts No. DE-FG-05-88ER40407, No. DE-AC02-05cch1123, No. DE-FG-ER40934, No. DE-AC05-00OR22725, No. DE-AC5207NA27344, and No. DE-FG02-95ER40939.

[1] T. J. Ross, Ph.D. thesis, University of Surrey, 2012.
[2] T. J. Ross, C. W. Beausang, R. O. Hughes, J. M. Allmond, C. T. Angell, M. S. Basunia, D. L. Bleuel, J. T. Burke, R. J. Casperson, J. E. Escher *et al.*, Phys. Rev. C **85**, 051304(R) (2012).
[3] T. J. Ross, R. O. Hughes, C. W. Beausang, J. M. Allmond, C. T. Angell, M. S. Basunia, D. L. Bleuel, J. T. Burke, R. J. Casperson, J. E. Escher *et al.*, Phys. Rev. C **88**, 031301(R) (2013).
[4] T. J. Ross, R. O. Hughes, J. M. Allmond, C. W. Beausang, C. T. Angell, M. S. Basunia, D. L. Bleuel, J. T. Burke, R. J. Casperson, J. E. Escher *et al.*, Phys. Rev. C **90**, 044323 (2014).
[5] F. S. Dietrich, I. J. Thompson, and T. Kawano, Phys. Rev. C **85**, 044611 (2012).
[6] S. Y. Chu, J. O. Rasmussen, M. A. Stoyer, L. F. Canto, R. Donangelo, and P. Ring, Phys. Rev. C **52**, 685 (1995).
[7] S. Y. Chu, J. O. Rasmussen, M. A. Stoyer, P. Ring, and L. F. Canto, Phys. Rev. C **52**, 1407 (1995).
[8] A. A. Shihab-Eldin, J. O. Rasmussen, M. A. Stoyer, D. G. Burke, and P. E. Garrett, Int. J. Mod. Phys. E **04**, 411 (1995).
[9] H. M. A. Radi, R. A. Mehrem, and J. O. Rasmussen, Phys. Rev. C **39**, 1340 (1989).
[10] J. M. Allmond, C. W. Beausang, J. O. Rasmussen, T. J. Ross, M. S. Basunia, L. A. Bernstein, D. L. Bleuel, W. Brooks, N. Brown, J. T. Burke *et al.*, Phys. Rev. C **81**, 064316 (2010).
[11] DWUCK (Distorted Wave University of Colorado Kunz) is a program written by Peter D. Kunz to calculate nuclear reaction cross sections numerically; A. Kiss, C. Mayer-Boricke, M. Rogge, P. Turek, and S. Wiktor, J. Phys. G: Nucl. Phys. **13**, 1067 (1987).
[12] CHUCK, A Coupled-channel program written by Peter D. Kunz to evaluate nuclear scattering amplitudes and differential collision cross sections; I. J. Thompson, Comput. Phys. Rep. **7**, 167 (1988).
[13] PTOLEMY is a program written by M. H. Macfarlane and Steven C. Pieper to compute nuclear elastic and direct-reaction cross sections for Heavy-Ion, Argonne National Laboratory, unpublished (1978); Shadi A. Bedoor, Ph.D. Dissertations, Western Michigan University, 2014.
[14] FRESCO is a program developed by Ian Thompson over the period 1983–2006, to perform coupled-reaction channels calculations in nuclear physics.
[15] W. D. Myers and K.-H. Schmidt, Nucl. Phys. A **410**, 61 (1983).
[16] R. Utama, Wei-Chia Chen, and J. Piekarewicz, J. Phys. G: Nucl. Part. Phys. **43**, 114002 (2016).
[17] P. Moller, J. R. Nix, W. D. Myers, and W. J. Swiatecki, At. Data Nucl. Data Tables **59**, 185 (1995).
[18] M. Centelles, X. Roca-Maza, X. Viñas, and M. Warda, Phys. Rev. Lett. **102**, 122502 (2009).
[19] I. Angeli and K. P. Marinova, At. Data Nucl. Data Tables **99**, 69 (2013).
[20] A. N. Antonov, M. K. Gaidarov, P. Sarriguren, and E. Moya de Guerra, Phys. Rev. C **94**, 014319 (2016).
[21] H. de Vries, C. W. de Jager, and C. de Vries, At. Data Nucl. Data Tables **36**, 495 (1987).
[22] D. Vautherin, Phys. Rev. C **7**, 296 (1973).
[23] L. C. Chamon, G. P. A. Nobre, D. Pereira, E. S. Rossi, Jr., C. P. Silva, L. R. Gasques, B. V. Carlson *et al.*, Phys. Rev. C **70**, 014604 (2004).
[24] Lie-Wen Chen, Che Ming Ko, and Bao-An Li, Phys. Rev. C **72**, 064309 (2005)
[25] K. Washiyama, K. Hagino, and M. Dasgupta, Phys. Rev. C **73**, 034607 (2006).
[26] C. M. Perey and F. G. Perey, At. Data Nucl. Data Tables **17**, 1 (1976).
[27] C. M. Perey and F. G. Perey, Phys. Rev. **132**, 755 (1963).
[28] A. De Shalit and H. Feshbach, *Theoretical Nuclear Physics: Nuclear Structure* (John Wiley, New York, 1974), Vol. 1; P. Marmier and E. Sheldon, *Physics of Nuclei and Particles* (Academic Press, San Diego, 1970), Vol. 2.
[29] R. B. Firestone, S. Y. Frank Chu, and C. M. Baglin, *Table of Isotopes*, 8th ed. (1999).
[30] A. Bäcklin, G. Hedin, B. Fogelberg, M. Saraceno, R. C. Greenwood, C. W. Reich, H. R Koch, H. A. Baader, H. D. Breitig, O. W. B. Schult *et al.*, Nucl. Phys. A **380**, 189 (1982).
[31] R. J. Ascuitto and N. K. Glendenning, Phys. Rev. **181**, 1396 (1969).
[32] R. J. Ascuitto and N. K. Glendenning, Phys. Rev. C **2**, 415 (1970).
[33] V. Bondarenko, A. V. Afanasjev, F. Bečvář, J. Honzátkoc, M.-E. Montero-Cabrera *et al.*, Nucl. Phys. A **726**, 175 (2003).
[34] A. J. Koning and J. P. Delaroche, Nucl. Phys. A **713**, 231 (2003).
[35] G. P. A. Nobre, A. Palumbo, M. Herman, D. Brown, S. Hoblit, and F. S. Dietrich, Phys. Rev. C **91**, 024618 (2015).

[36] A. Wallner, T. Belgya, M. Bichler, K. Buczak, I. Dillmann *et al.*, Phys. Rev. Lett. **112**, 192501 (2014).
[37] V. Margerin, G. Lotay, P. J. Woods, M. Aliotta, G. Christian *et al.*, Phys. Rev. Lett. **115**, 062701 (2015).
[38] A. Deltuva, A. Ross, E. Norvaišas, and F. M. Nunes, Phys. Rev. C **94**, 044613 (2016).
[39] S. J. Waldecker and N. K. Timofeyuk, Phys. Rev. C **94**, 034609 (2016).
[40] Q. Ducasse, B. Jurado, M. Aïche, P. Marini, L. Mathieu, A. Görgen, M. Guttormsen, A. C. Larsen, T. Tornyi, J. N. Wilson *et al.*, Phys. Rev. C **94**, 024614 (2016).
[41] K. G. Leach, P. E. Garrett, G. C. Ball, P. C. Bender, V. Bildstein *et al.*, Phys. Rev. C **94**, 011304(R) (2016).
[42] P. Humby, A. Simon, C. W. Beausang, J. M. Allmond, J. T. Burke, R. J. Casperson, R. Chyzh, M. Dag, K. Gell, R. O. Hughes *et al.*, Phys. Rev. C **94**, 064314 (2016).
[43] K. Nowak, K. Wimmer, S. Hellgartner, D. Mücher, V. Bildstein *et al.*, Phys. Rev. C **93**, 044335 (2016).
[44] A. O. Macchiavelli, H. L. Crawford, C. M. Campbell, R. M. Clark, M. Cromaz *et al.*, Phys. Rev. C **94**, 051303(R) (2016).
[45] G. W. Bailey, N. K. Timofeyuk, and J. A. Tostevin, Phys. Rev. C **95**, 024603 (2017).
[46] G. Løvhøiden and D. G. Burke, Can. J. Phys. **53**, 1182 (1975).
[47] J. Rekstad, B. Nordmoen, A. Henriques, F. Ingebretsen, S. Messelt, T. F. Thorsteinsen, and E. Hammarén, Nucl. Phys. A **417**, 376 (1984).
[48] T. S. Tveter, M. Guttormsen, J. Rekstad, J. Kownacki, and T. F. Thorsteinsen, Nucl. Phys. A **516**, 1 (1990).
[49] Y. Fujita, H. Fujita, T. Adachi, G. Susoy, A. Algora *et al.*, Phys. Rev. C **91**, 064316 (2015).
[50] E. Ganioğlu, H. Fujita, B. Rubio, Y. Fujita, T. Adachi, A. Algora, M. Csatlós, J. M. Deaven, E. Estevez-Aguado, C. J. Guess *et al.*, Phys. Rev. C **93**, 064326 (2016).
[51] D. Frekers, M. Alanssari, T. Adachi, B. T. Cleveland, M. Dozono, H. Ejiri, S. R. Elliott, H. Fujita, Y. Fujita, M. Fujiwara *et al.*, Phys. Rev. C **94**, 014614 (2016).